





Article

Utilizing the Intrinsic Thermal Instability of Swedenborgite Structured $\text{YBaCo}_4\text{O}_{7+\delta}$ as an Opportunity for Material Engineering in Lithium-Ion Batteries by Er and Ga Co-Doping Processes

Sanghyuk Park ^{1,†}, Kwangho Park ^{2,†}, Ji-Seop Shin ², Gyeongbin Ko ¹, Wooseok Kim ¹, Jun-Young Park ^{2,*} and Kyungjung Kwon ^{1,*}

¹ Department of Energy & Mineral Resources Engineering, Sejong University, Seoul 05006, Korea; shpark@sejong.ac.kr (S.P.); radsfl@naver.com (G.K.); kevin5588@naver.com (W.K.)

² HMC, Department of Nanotechnology and Advanced Materials Engineering, Sejong University, Seoul 05006, Korea; beongae430@naver.com (K.P.); sjs93623@nate.com (J.-S.S.)

* Correspondence: jyoung@sejong.ac.kr (J.-Y.P.); kfromberk@gmail.com (K.K.); Tel.: +82-2-3408-3947 (K.K.)

† These authors contributed equally to this work.

Abstract: We firstly introduce Er and Ga co-doped swedenborgite-structured $\text{YBaCo}_4\text{O}_{7+\delta}$ (YBC) as a cathode-active material in lithium-ion batteries (LIBs), aiming at converting the phase instability of YBC at high temperatures into a strategic way of enhancing the structural stability of layered cathode-active materials. Our recent publication reported that $\text{Y}_{0.8}\text{Er}_{0.2}\text{BaCo}_{3.2}\text{Ga}_{0.8}\text{O}_{7+\delta}$ (YEBCG) showed excellent phase stability compared to YBC in a fuel cell operating condition. By contrast, the feasibility of the LiCoO_2 (LCO) phase, which is derived from swedenborgite-structured YBC-based materials, as a LIB cathode-active material is investigated and the effects of co-doping with the Er and Ga ions on the structural and electrochemical properties of Li-intercalated YBC are systemically studied. The intrinsic swedenborgite structure of YBC-based materials with tetrahedrally coordinated $\text{Co}^{2+}/\text{Co}^{3+}$ are partially transformed into octahedrally coordinated Co^{3+} , resulting in the formation of an LCO layered structure with a space group of $R-3m$ that can work as a Li-ion migration path. Li-intercalated YEBCG (Li[YEBCG]) shows effective suppression of structural phase transition during cycling, leading to the enhancement of LIB performance in Coulombic efficiency, capacity retention, and rate capability. The galvanostatic intermittent titration technique, cyclic voltammetry and electrochemical impedance spectroscopy are performed to elucidate the enhanced phase stability of Li[YEBCG].

Keywords: Li-ion battery; cathode material; swedenborgite; co-doping; phase stability



Citation: Park, S.; Park, K.; Shin, J.-S.; Ko, G.; Kim, W.; Park, J.-Y.; Kwon, K. Utilizing the Intrinsic Thermal Instability of Swedenborgite Structured $\text{YBaCo}_4\text{O}_{7+\delta}$ as an Opportunity for Material Engineering in Lithium-Ion Batteries by Er and Ga Co-Doping Processes. *Materials* **2021**, *14*, 4565. <https://doi.org/10.3390/ma14164565>

Academic Editor: Zhenghong Huang

Received: 12 July 2021

Accepted: 11 August 2021

Published: 14 August 2021

Publisher's Note: MDPI stays neutral with regard to jurisdictional claims in published maps and institutional affiliations.



Copyright: © 2021 by the authors. Licensee MDPI, Basel, Switzerland. This article is an open access article distributed under the terms and conditions of the Creative Commons Attribution (CC BY) license (<https://creativecommons.org/licenses/by/4.0/>).

1. Introduction

Recent research for cathode-active materials in the field of lithium-ion batteries (LIBs) pursues high energy density with a long cycle life, which has been triggered by the worldwide growth of the electric vehicle (EV) market. Ni-rich layered cathode-active materials, such as $\text{LiNi}_{1-x-y}\text{Mn}_x\text{Co}_y\text{O}_2$ (NMC) and $\text{LiNi}_{1-x-y}\text{Co}_x\text{Al}_y\text{O}_2$ (NCA), have received a great deal of attention due to their higher energy density with moderate cycling stability in the wide range of operating conditions compared to other types of cathode-active materials with olivine- (LiFePO_4) or spinel- (LiMn_2O_4) structures [1]. The well-known LiCoO_2 (LCO), which has the same layered crystal structure as NMC (space group: $R-3m$) and has been widely used mainly in portable IT devices and power tools in recent decades, became a minor option as EV battery cathode material owing to its limited practical capacity characteristics. Specifically, LCO undergoes severe structural distortion constraining the practical capacity when cycled above 4.2 V vs. Li/Li^+ [2]. Thus, a proper cathode active material for EV requires a high Ni content in its chemical composition to

satisfy high energy density despite the detrimental effect of the Ni ions on structural and thermal stability. Accordingly, many researchers have made a variety of efforts to find new dopants or surface coating compounds to suppress the severe structural degradation of Ni-rich layered cathode active materials during cycling, notwithstanding the role of Mn and Al species for structural stabilization in NMC and NCA, respectively [3–14]. This is mainly due to a specific phase transition region from H2 to H3 at around 4.2 V vs. Li/Li⁺, which leads to abrupt lattice contraction causing particle pulverization induced by microcracks [15,16].

On the other hand, Co-containing swedenborgite-structured YBaCo₄O_{7+δ} (YBC) materials with significantly large oxygen-storage capacity are considered to be promising catalysts in solid oxide fuel cells (SOFC) working at intermediate temperatures [17,18]. It is well known that the swedenborgite structure (space group: *P6₃mc*) of YBC with two layers of CoO₄ tetrahedral coordinates suffers from severe phase instability by thermal decomposition at 600–800 °C due to the preference of Co ions for octahedral coordination, which makes its application in SOFC difficult [19,20]. Manthiram et al. reported that YBC doped with the optimum content of Ga, which substitutes for Co sites, can effectively overcome this phase instability at high temperatures of 600–800 °C [21]. Our recent work reported that Er and Ga co-doped YBC oxide (YEBCG) showed excellent phase stability compared to YBC, presenting long-term durability under reversible protonic ceramic cell conditions [22]. Meanwhile, there are a few reports adopting Er or Ga as dopants for cathode-active materials in LIBs. While Er-doped LiFePO₄ and LiNi_{0.5}Mn_{1.5}O₄ showed improved cycling stability [23,24], Ga-doped layered LiNi_{0.6}Co_{0.2}Mn_{0.2}O₂ presented enhanced electrochemical performance and thermal stability, which is in line with the Manthiram group's result based on the YBC material related to the improved phase stability at high temperatures [21,25].

Inspired by these results, we herein introduced Er and Ga co-doped swedenborgite-structured YBC as a cathode-active material in LIBs, aiming at converting the issue of phase instability of YBC at high temperatures into a challenge to explore a way towards enhancing the structural stability of layered cathode-active materials. The high temperature (800 °C) calcination process for Li-ion intercalation into the swedenborgite structure did not decompose the intrinsic swedenborgite structure of YBC and YEBCG, and forms merely a few secondary phases induced by partial thermal decomposition and a layered LCO phase, which locates Co in octahedral coordinates. The feasibility of the LCO phase, which is derived from the swedenborgite-structured YBC-based materials, as a layered cathode-active material for the LIBs was investigated, and the effects of co-doping with the Er and Ga ions on the structural and electrochemical properties of Li-intercalated YBC were studied in detail.

2. Experimental Section

2.1. Synthesis and Characterization of Materials

To prepare YBC and YEBCG powders, stoichiometric Ba(NO₃)₂ (99.95%, metal basis Alfa Aesar), Er(NO₃)₃·5H₂O (99.9%, Alfa Aesar), Y(NO₃)₃·6H₂O (99.9%, Alfa Aesar), (NH₄)₂Ce(NO₃)₆ (99.99%, Alfa Aesar), and Ga(NO₃)₃·xH₂O (99.9%, metal basis, Alfa Aesar) were dissolved in distilled water with glycine as a combusting fuel and then heated on a heating plate (MSH-20D, DAIHAN Scientific Co., Ltd., Wonju, Korea) at 350 °C until the metal nitrates converted into black ashes. After the combustion, the ashes were ground with a mortar and then calcined at 1000 °C for 12 h under an air atmosphere to obtain a single-phased crystalline [22]. In order to identify the crystal structure of the YBC-based materials, an X-ray diffraction (XRD) technique (X'Pert, PANalytical, Cu K α radiation, Almelo, The Netherlands) was carried out with a step size of 0.026° in a 2 θ range from 10 to 80°. Utilizing the XRD data, the FullProf software was used for Rietveld refinement to yield lattice parameters. The morphological characterization of the YBC-based materials was performed using a field emission scanning electron microscope (FE-SEM, SU-8010, Hitachi Ltd., Tokyo, Japan) with energy-dispersive X-ray spectroscopy

(EDS). To measure the Brunauer-Emmett-Teller (BET) surface area, nitrogen gas was used for an adsorption/desorption method (BELSORP-max, BEL Inc., Leitchfield, KY, USA) at 77 K to remove residual impurities and moisture with an average mass of 0.54 g for each specimen. For the sake of Li-intercalation, the synthesized YBC and YEBCG were mixed with LiOH·H₂O in a molar ratio of 1:1.1, followed by calcination under air atmosphere for 10 h at 800 °C. The Li-intercalated YBC and YEBCG oxides are referred to as Li[YBC] and Li[YEBCG], respectively.

2.2. Electrochemical Analysis

For a cathode slurry, the Li[YBC] and Li[YEBCG] cathode active materials, carbon black (Super-P) as a conducting material, and polyvinylidene fluoride (KF 1100) as a binder in a weight ratio of 80:10:10 were thoroughly mixed in a N-methylpyrrolidinone (NMP) solution with 30% solid content and casted on Al foil as a current collector. Electrochemical properties were investigated using CR2032-type coin cells, which were fabricated in a moisture-controlled glove box under an argon atmosphere. While 1 M LiPF₆ dissolved in a mixture of ethyl methyl carbonate and ethylene carbonate (2:1, *v/v*) was used as an electrolyte, Li metal foil and polyethylene film were used as anode and separator, respectively. Cycling stability was assessed by cycling the cells at 0.1 C (46 mA g⁻¹ as 1 C) in different potential ranges of 2.0 to 4.5 V for 50 cycles and 2.5 to 4.3 V for 100 cycles, while a rate capability test was conducted in the potential range from 2.0 to 4.5 V in various C-rate conditions using a battery cyler (WBCS3000L, WonAtech Ltd., Seoul, Korea) at 25 °C. For activating the cells, cycling at 0.1 C during initial two cycles was conducted prior to the electrochemical tests as a formation step. Electrochemical impedance spectroscopy (EIS) and cyclic voltammetry (CV) were performed using a potentiostat system (versaSTAT 3, AMETEK Inc., Berwyn, PA, USA) to compare the change in internal cell resistance and the degree of overpotentials during cycling, respectively. A galvanostatic intermittent titration technique (GITT) was conducted to calculate Li-ion diffusion coefficients. All the values of potentials were based on Li/Li⁺ in this study unless otherwise mentioned.

3. Results and Discussion

The XRD patterns of swedenborgite-structured YBC and YEBCG before and after the Li-ion intercalating calcination process at 800 °C are presented in Figure 1. It is known that BaCoO_{3-δ} and Y₂O₃ secondary phases can form readily due to oxidative thermal decomposition from the intrinsic YBC structure above 600 °C [26]. This structural degradation of Li[YEBCG] induced by the thermal decomposition was mitigated when Er and Ga were co-doped in the YBC structure. As seen in Figure 1, the peak intensity of secondary phases was reduced for Li[YEBCG], indicating the better structural stability at the oxidative high temperature than Li[YBC]. A LiCoO₂ phase allowing the (de)intercalation of Li ions was also newly formed (marked as green-colored symbols in the figure), which might be ascribed to the evolution of Co ions located at octahedral coordinates during the calcination process. Likewise, the Co ions in BaCoO₃ (marked as gray-colored symbols in the figure), which is a main decomposition product of YBC, have octahedral coordination [27], whereas the Co ions in YBC have a tetrahedral coordination. Meanwhile, Table 1 lists the crystal lattice parameters of pristine YBC and YEBCG, showing the increased lattice parameters of a- and c-axes with larger lattice volume for YEBCG compared to YBC, which is consistent with the previous literature [22].

Table 1. Crystallographic parameters of YBC and YEBCG calculated by Rietveld refinement.

	YBC	YEBCG
a-axis (Å)	6.2993	6.3097
c-axis (Å)	10.2534	10.2674
Volume (Å ³)	352.3540	354.0059

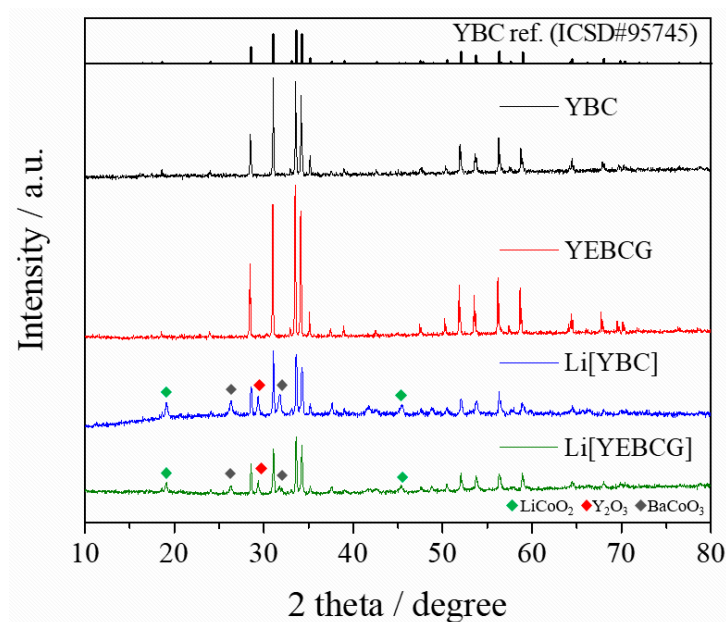


Figure 1. XRD patterns of pristine YBC and YEBCG, and their Li-intercalated forms of Li[YBC] and Li[YEBCG].

To elucidate the relationship between changes in structural phase and morphology before and after the Li-intercalation process, a FE-SEM analysis was performed. Figure 2 shows the surface morphology of YBC, Li[YBC], YEBCG, and Li[YEBCG]. Compared to the pristine particles, the Li-intercalated Li[YBC] and Li[YEBCG] samples exhibited a negligible change in morphology. It can be concluded that the aforementioned phase deformation induced by the oxidative thermal decomposition does not affect the morphological change from their original shapes. Meanwhile, the elemental mapping data of Li[YBC] and Li[YEBCG] are presented, as shown in Figure 3a for Li[YBC] and Figure 3b for Li[YEBCG], respectively, indicating that all of constituent elements were evenly distributed.

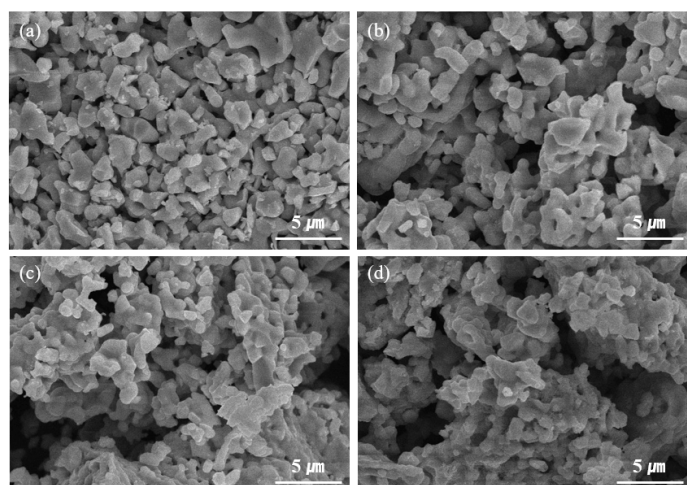


Figure 2. FE-SEM images of (a) YBC, (b) Li[YBC], (c) YEBCG, and (d) Li[YEBCG].

Figure 4a,b display the initial charge (delithiation) and discharge (lithiation) curves of Li[YBC] and Li[YEBCG] cathode active materials. Li[YEBCG] showed increased charge/discharge capacities with enhanced Coulombic efficiency compared to Li[YBC]. A differential capacity analysis was performed in order to look into the phase transition behavior during the initial cycle in a potential range of 2.0–4.5 V, as shown in Figure 4c,d, which was derived from the initial charge/discharge curves. Two minor peaks between 4.05 and

4.25 V were observed in Li[YBC] besides the major peaks at around 3.9 V, whereas the phase transition was effectively suppressed in the case of Li[YEBCG], indicating the enhanced structural stability. These electrochemical behaviors of Li[YBC] and Li[YEBCG] are consistent with the typical phase transition behavior of the LCO cathode active materials in LIBs [2]. Because these phase transitions during a repetitive cycling, specifically above 4.2 V, can bring about the deterioration of LIB performance, the mitigation of the phase transition is a crucial issue for layered cathode active materials [15]. Consequently, LIB performance including the cycle life and the rate capability of Li[YEBCG] is expected to outperform Li[YBC] considering the structural and electrochemical features of enlarged lattice volume and suppressed phase stability.

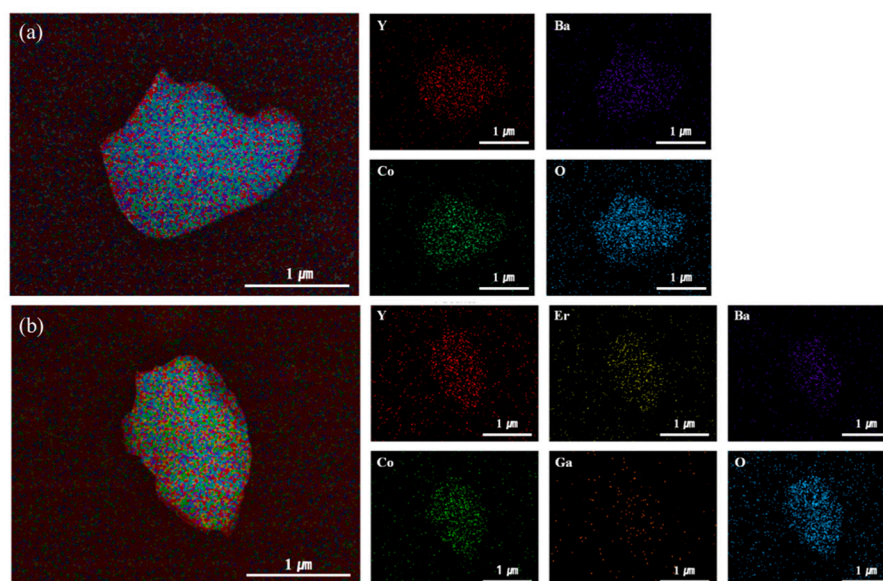


Figure 3. Elemental mapping images of (a) Li[YBC] and (b) Li[YEBCG] analyzed by EDS.

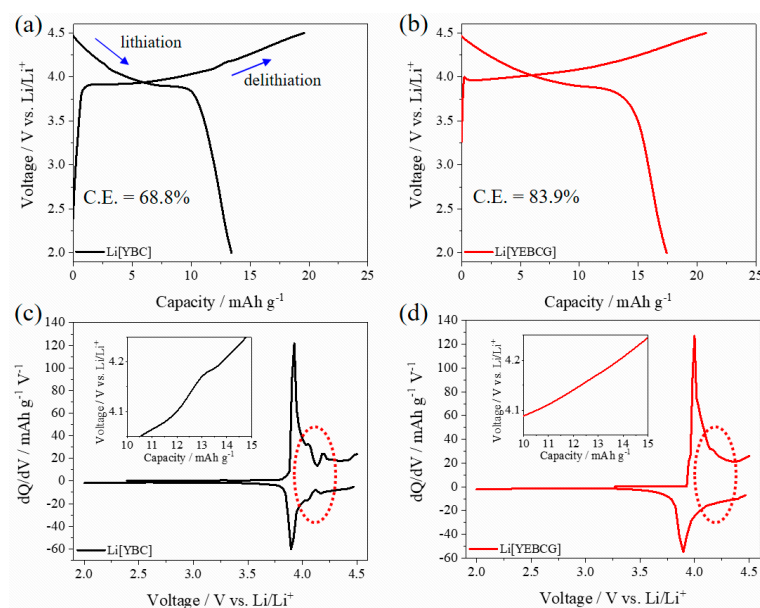


Figure 4. (a,b) Initial charge/discharge and (c,d) differential capacity curves of Li[YBC] and Li[YEBCG], respectively. A distinct phase transition region (red-dotted circles in (c,d)) in the potential around 4.2 V was displayed with insets of the corresponding voltage profile. (C.E.: Coulombic efficiency).

Figure 5 presents the cycle performance of the cathode active materials for 50 cycles at 0.1 C in a potential range of 2.0–4.5 V. The capacity retention of Li[YBC] was drastically

aggravated right after the initial cycle and reached less than 10% after about 20 cycles. By contrast, Li[YEBCG] showed superior capacity retention with a relatively stable feature of Coulombic efficiency over the entire cycling process. After 50 cycles, Li[YEBCG] had a capacity retention of 50%, which was about ten times higher than Li[YBC]. The corresponding voltage profiles of Li[YBC] (see Figure 5b) clearly showed rapid capacity fading with increasing overpotentials during cycling, while Li[YEBCG] presented a feature of mitigated capacity fading (see Figure 5c), indicating the positive effects of co-doping with Er and Ga on the suppression of the undesired phase transition as aforementioned in Figure 4. Long-term cycle performance was additionally conducted in the potential range of 2.5–4.3 V in Figure S1, which is closer to the practical operating condition of LIBs including a constant voltage charging step with a moderate charging cut-off potential. The long-term cycle performance showed relatively enhanced cycling stability compared to the 4.5 V cut-off condition resulting from a limited (de)lithiation range, which led to decreased discharge capacities for both samples. In general, a higher upper cut-off potential shows higher capacities at the expense of cycling stability [28].

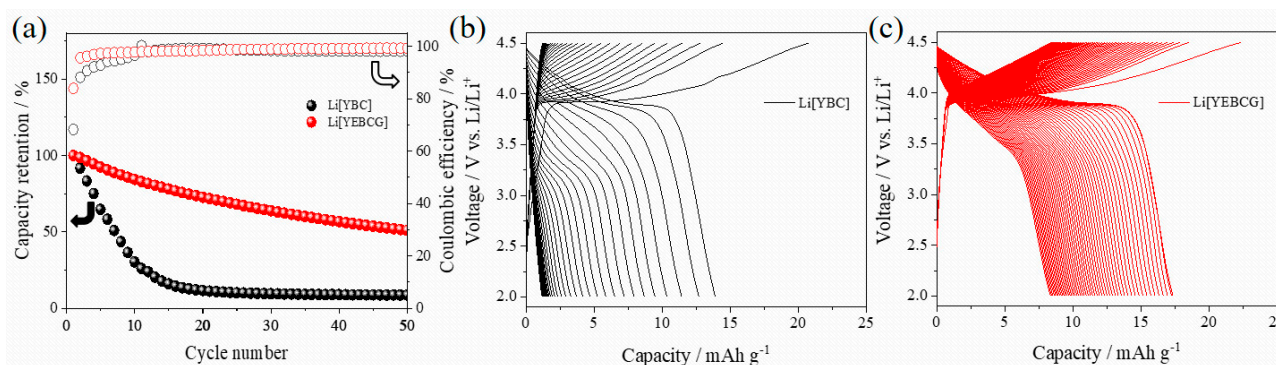


Figure 5. (a) Capacity retention at 0.1 C with Coulombic efficiency, and corresponding voltage profiles of (b) YBC and (c) YEBCG during 50 cycles.

In order to electrochemically elucidate a specific reason for the improved capacity retention of Li[YEBCG], the EIS was conducted in a frequency range from 0.01 Hz to 1 MHz with an alternating voltage amplitude of 15 mV. The EIS technique in LIBs is considered as one of the most attractive analytical tools that can separate and quantify cell resistance in-situ, avoiding any impact of moisture or oxygen on sensitive samples [29]. Figure 6 shows the resulting Nyquist plots of Li[YBC] and Li[YEBCG] with an increasing cycle number under a pseudo-equilibrium state for charged cells. Li[YBC] has shown extremely larger impedance growth than Li[YEBCG] after the formation step. Noticeably, the first semicircles in a high frequency region that are related to the film resistance induced by the formation of solid electrolyte interphase (SEI) between electrodes and electrolytes gradually shrank with an increased cycle number from 10 to 50 in both samples (see the insets in the figures). It is hard to intuitively interpret the abnormal phenomenon about the gradual decrease of film resistance, which is contrary to other relevant research [30,31]. In the meantime, the second semicircles in a low frequency region regarding charge transfer resistance (R_{ct}) indicated incremental trends in both samples during cycling due to the structural degradation of the cathode active materials. In addition, this might correlate with the intrinsically weak adhesion property of YBC-based materials to current collectors (see Figure S2). Therefore, it can be concluded that the poor capacity retention of Li[YBC] was caused by severe impedance growth in the cell, while the doping with Er and Ga is deemed to be a crucial factor to reinforce the host structure and facilitate the charge transfer process in the Li[YEBCG] structure.

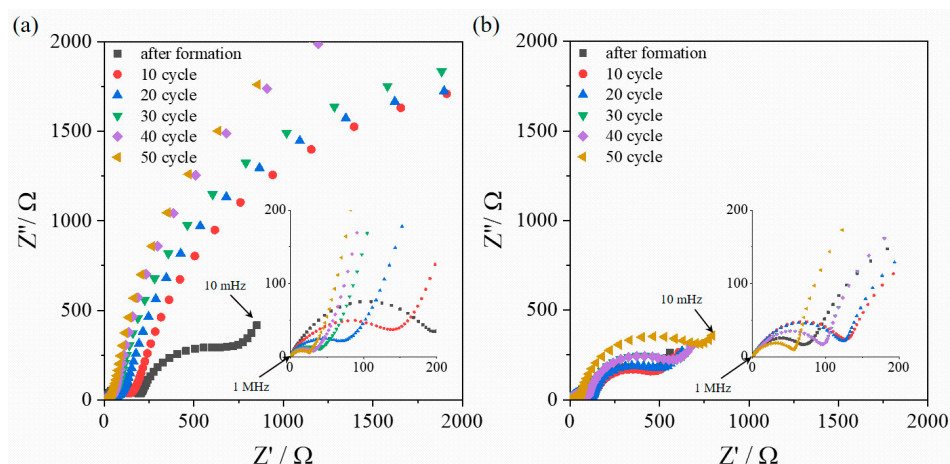


Figure 6. Nyquist plots of (a) Li[YBC] and (b) Li[YEBCG] with increasing cycle numbers.

Through a series of EIS and CV measurements under various electrochemical conditions, the superior electrochemical performance of Li[YEBCG] compared to that of Li[YBC] was clearly confirmed again. As seen in Figure 7a, the EIS results obtained at equilibrium states before the following CV tests showed that Li[YBC] has a relatively lowered R_{ct} value than that of Li[YEBCG], which leads to a slightly reduced potential intervals (ΔV) between main anodic and cathodic peaks compared with Li[YEBCG] as shown in Figure 7b. Although the ΔV generally indicates the reversibility of Li-ion (de)intercalation, the obvious feature of the suppressed phase transition of Li[YEBCG] during the cycling at 0.1 mV s^{-1} positively affected the repetitive CV measurements at 0.5 mV s^{-1} as shown in Figure 7c,d. Li[YBC] presented a different electrode polarization induced by severe overpotentials after 10 cycles leading to the increase in ΔV , whereas the degree of overpotentials for Li[YEBCG] was slightly changed after 10 cycles representing the enhancement of structural stability of Li[YEBCG] by the Er and Ga co-doping process. It is worth noting that the R_{ct} value of Li[YEBCG] measured after the formation step became smaller than Li[YBC] (see Figure 6).

The EIS and CV measurements were additionally conducted at a different temperature of 60°C , as displayed in Figure 7e,f, respectively. Compared with the results at 25°C , the R_{ct} values have drastically decreased in both samples, which might be attributed to the effect of elevated temperature facilitating the migration of Li^+ ions in the bulk structure. In the CV data, the overpotentials of both samples were also reduced. Interestingly, the feature of severe phase transition of Li[YBC] during the CV measurement at 0.1 mV s^{-1} completely disappeared, which could lead to the improvement of structural stability during the cycling. Although the capacity retention of Li[YEBCG] at 60°C was indeed improved in comparison with that at 25°C , the drastic aggravation of capacity retention after the initial cycle was still a problematic issue (see Figure S3).

The rate capability tests of Li[YBC] and Li[YEBCG] were performed to look into the kinetic behavior during reversible (de)lithiation reactions at different discharging C-rates with a fixed charging C-rate of 0.1 C, as shown in Figure 8a,b. Whereas the overpotentials of Li[YBC] rapidly increased along with the decrease in operating voltage as the C-rate increases, Li[YEBCG] presented a much better rate performance than Li[YBC]. Moreover, given that the decay tendency in the charge capacity of Li[YEBCG] was apparently mitigated compared with Li[YBC], it can be understood that the intrinsic swedenborgite structure of Li[YEBCG] is effectively stabilized by the co-doping with Er and Ga. Figure 8c shows the relative capability of the samples with respect to discharge capacities at various C-rates compared to the discharge capacity at 0.1 C. Li[YEBCG] had superior relative capability to that of Li[YBC] as the C-rate increases, also suggesting that the Er and Ga co-doped host structure of YEBCG is favorable for Li ions to migrate into the bulk structure.

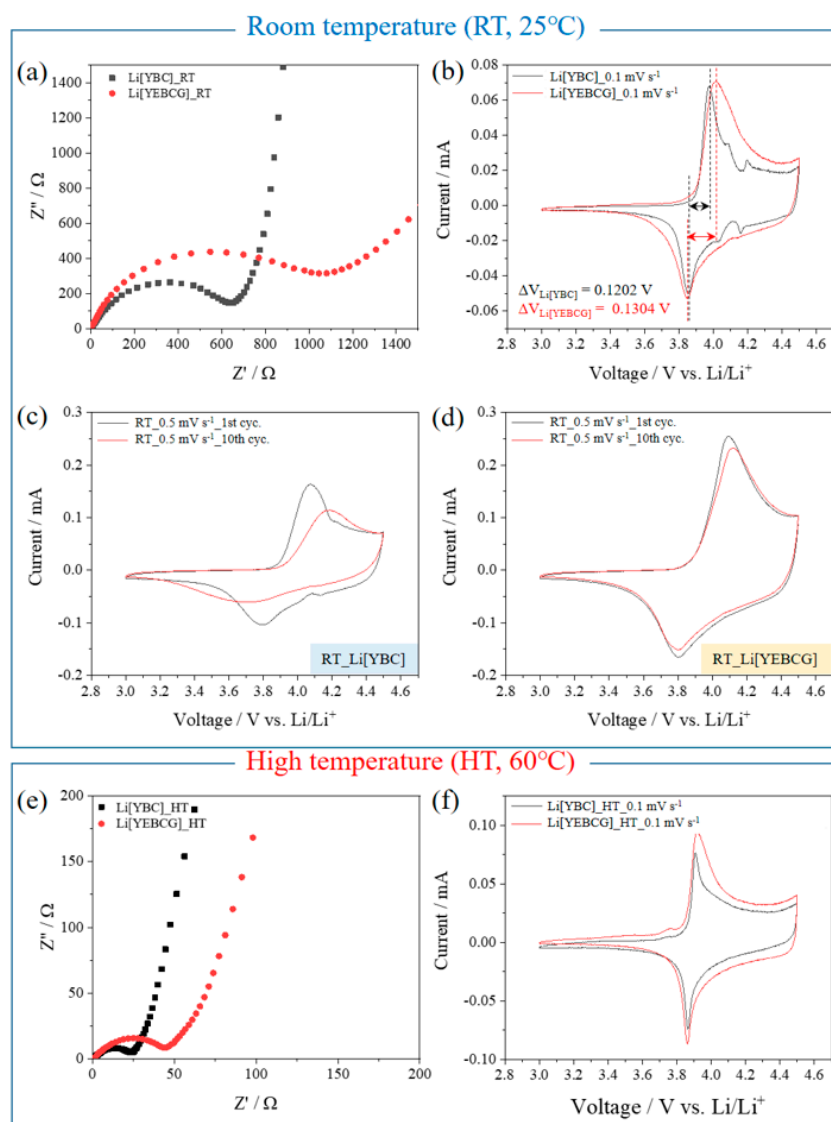


Figure 7. Nyquist plots and CV curves of Li[YBC] and Li[YEBCG] under various experimental conditions. (a,e) EIS data before the CV tests at equilibrium states, (b,f) initial CV curves at 0.1 mV s⁻¹, and (c,d) CV curves during the 1st and 10th cycles at 0.5 mV s⁻¹, where (a–d) were tested at 25 °C and (e,f) at 60 °C.

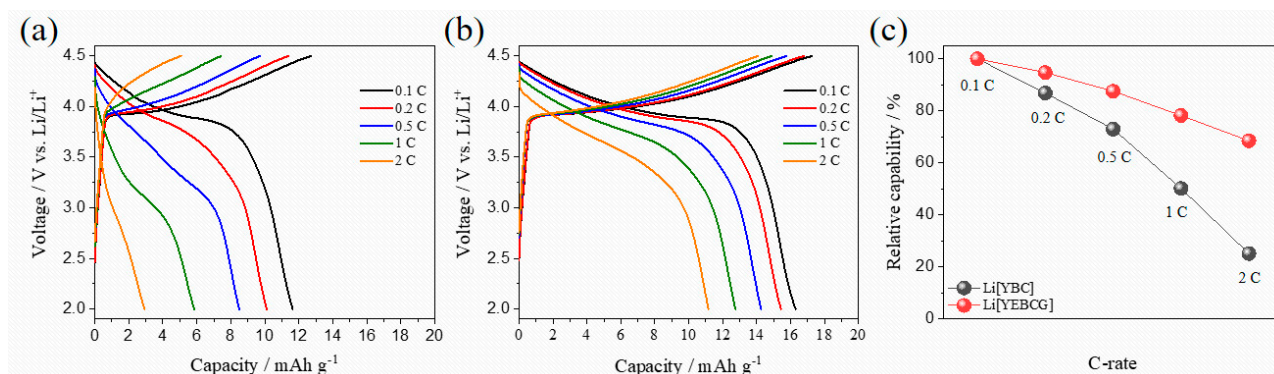


Figure 8. Rate capability of (a) Li[YBC] and (b) Li[YEBCG], and (c) their relative capability at various discharging C-rates from 0.1 to 2 C with a fixed charging C-rate of 0.1 C.

Lastly, to compare the Li-ion diffusion coefficients (D_{Li^+}) between the samples, a GITT analysis was carried out as shown in Figure 9. GITT curves shown in Figure 9a were obtained during the second charging process, and a single titration step was described in Figure 9b, where ΔE_s (V) is the voltage change between steady states and ΔE_τ (V) is the total change of cell voltage in a single titration step [32]. Fick's second law is utilized to calculate the D_{Li^+} as below [33]:

$$D_{\text{Li}^+} = \frac{4}{\pi} \left(\frac{mV}{MS} \right)^2 \left(\frac{\Delta E_s}{\tau \left(\frac{dE_\tau}{d\sqrt{\tau}} \right)} \right)^2 \quad \left(\tau \ll \frac{L^2}{D_{\text{Li}^+}} \right) \quad (1)$$

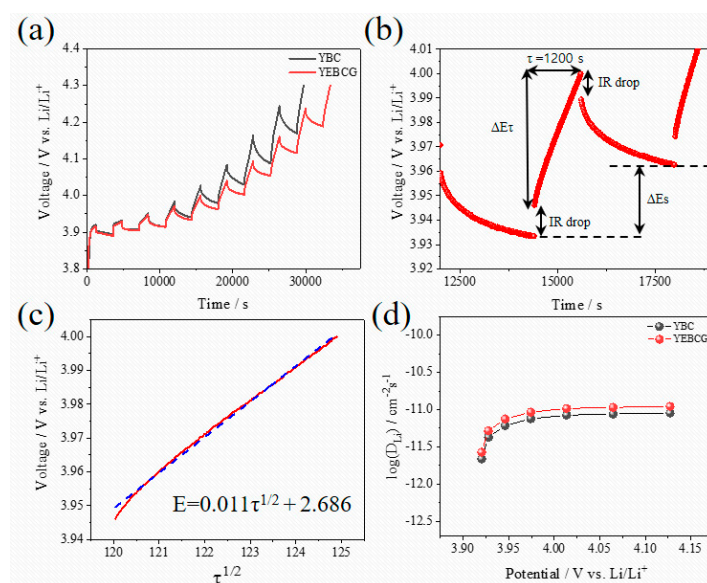


Figure 9. (a) GITT curves of Li[YBC] and Li[YEBCG] during the second charge process at a current density of 4.6 mA g^{-1} . (b) GITT curve at a single titration step of Li[YEBCG] with (c) corresponding linear behavior in the relationship of E vs. $\tau^{1/2}$. (d) Li-ion diffusion coefficients of Li[YBC] and Li[YEBCG] calculated from the GITT curves as a function of the cell potential.

As seen in Figure 9c, under the assumption that E vs. $\sqrt{\tau}$ shows a straight-line behavior during the titration step, Equation (1) can be simplified into Equation (2) [34,35],

$$D_{\text{Li}^+} = \frac{4}{\pi\tau} \left(\frac{mV}{MS} \right)^2 \left(\frac{\Delta E_s}{\Delta E_\tau} \right)^2 \quad \left(\tau \ll \frac{L^2}{D_{\text{Li}^+}} \right) \quad (2)$$

where m is the mass (g), V is the molar volume ($\text{cm}^3 \text{ mol}^{-1}$), and M is the molecular weight (g mol^{-1}) of cathode active materials. S is the contact area (cm^2) between electrodes and electrolytes, and L is the Li-ion diffusion length (cm).

The D_{Li^+} values of samples calculated using Equation (2) were plotted as a function of cell potential, showing relatively higher D_{Li^+} values of Li[YEBCG] compared to Li[YBC] over the entire potential range (Figure 9d). It can be explained that Li[YEBCG] has better kinetic behavior for the (de)intercalation of Li ions compared to Li[YBC] regardless of C-rate conditions due to the higher D_{Li^+} . Therefore, the comprehensively improved electrochemical properties of Li[YEBCG] are clearly attributed to the effect of cationic substitution of Er and Ga that stabilize the host structure from undesired phase transition.

4. Conclusions

We synthesized Er and Ga co-doped swedenborgite-structured YBC, which was utilized as a cathode-active material to investigate the potential enhancement of phase stability. The peak intensity of secondary phases in the XRD patterns was mitigated in the case

of Li[YEBCG], indicating the better structural stability at the oxidative high temperature compared with Li[YBC]. A LiCoO₂ phase allowing the (de)intercalation of Li ions was also newly formed, which might result from the evolution of Co ions located at octahedral coordinates during the calcination process. The partial thermal deformation resulting from oxidative calcination barely affected the morphologies and their elemental distribution of YBC and YEBCG. Regarding the LIB performance, Li[YEBCG] exhibited superior capacity retention with enhanced charge/discharge capacities compared to Li[YBC], showing the mitigated feature of phase transition at around 4.2 V. The poor capacity retention of Li[YBC] was ascribed to severe impedance growth during cycling, while the doping with Er and Ga was considered to be a crucial factor to reinforce the host structure and facilitate the charge transfer process in the Li[YEBCG] structure, leading to the effective suppression of impedance growth. Whereas the overpotentials of Li[YBC] rapidly increased along with the decrease in operating voltage as the C-rate increased, Li[YEBCG] showed much better rate performance than Li[YBC]. The calculated D_{Li^+} of samples showed the relatively higher D_{Li^+} values of Li[YEBCG] compared to Li[YBC] over the entire potential range, explaining that Li[YEBCG] has better kinetic behavior for the (de)intercalation of Li ions than Li[YBC] regardless of C-rate conditions. Consequently, the comprehensively improved electrochemical properties of Li[YEBCG] are clearly attributed to the enhanced phase stability induced by the stabilizing effect of Er and Ga co-doping on the host structure from the undesired phase transition. Future work will include the influence of Er and Ga co-doping in more conventional LIB cathode active materials on the mitigation of structural degradation during cycling.

Supplementary Materials: The following are available online at <https://www.mdpi.com/article/10.3390/ma14164565/s1>, Figure S1: Initial charge/discharge curves and long-term cycle performance of Li[YBC] and Li[YEBCG] in a potential range of 2.5–4.3 V, Figure S2: Comparative pictures of (a) Li[YBC] and (b) Li[YEBCG] after the cycling test, Figure S3: Cycle performance of Li[YBC] at different temperatures of 25 and 60 °C.

Author Contributions: Conceptualization, S.P. and K.P.; methodology, S.P. and J.-S.S.; validation, G.K. and W.K.; investigation, G.K. and W.K.; writing—original draft preparation, S.P. and K.P.; writing—review and editing, K.K.; supervision, K.K. and J.-Y.P.; project administration, J.-Y.P. and J.-S.S. All authors have read and agreed to the published version of the manuscript.

Funding: This work was supported by Basic Science Research Program and the Next-generation Engineering Researchers Development Program (2019H1D8A2106002) through the National Research Foundation of Korea (NRF) funded by the Ministry of Education (2020R1A6A1A03038540, 2021R1I1A1A01044063), the Ministry of Science and ICT (2020R1F1A1053911), and the Korea Ministry of Environment (MOE) as ‘Graduate School specialized in Climate Change’.

Institutional Review Board Statement: Not applicable.

Informed Consent Statement: Not applicable.

Data Availability Statement: The data presented in this study are available on request from the corresponding author.

Conflicts of Interest: The authors declare no conflict of interest.

References

1. Li, W.; Erickson, E.M.; Manthiram, A. High-Nickel Layered Oxide Cathodes for Lithium-Based Automotive Batteries. *Nat. Energy* **2020**, *5*, 26–34. [[CrossRef](#)]
2. Xia, H.; Lu, L.; Meng, Y.S.; Ceder, G. Phase Transitions and High-Voltage Electrochemical Behavior of LiCoO₂ Thin Films Grown by Pulsed Laser Deposition. *J. Electrochem. Soc.* **2007**, *154*, A337–A342. [[CrossRef](#)]
3. Weigel, T.; Schipper, F.; Erickson, E.M.; Susai, F.A.; Markovsky, B.; Aurbach, D. Structural and Electrochemical Aspects of LiNi_{0.8}Co_{0.1}Mn_{0.1}O₂ Cathode Materials Doped by Various Cations. *ACS Energy Lett.* **2019**, *4*, 508–516. [[CrossRef](#)]
4. Trease, N.M.; Seymour, I.D.; Radin, M.D.; Liu, H.; Hy, S.; Chernova, N.; Parikh, P.; Devaraj, A.; Wiaderek, K.M.; Chupas, P.J.; et al. Identifying the Distribution of Al³⁺ in LiNi_{0.8}Co_{0.15}Al_{0.05}O₂. *Chem. Mater.* **2016**, *28*, 8170–8180. [[CrossRef](#)]
5. Sivaprakash, S.; Majumder, S.B. Understanding the Role of Zr⁴⁺ Cation in Improving the Cycleability of LiNi_{0.8}Co_{0.15}Zr_{0.05}O₂ Cathodes for Li Ion Rechargeable Batteries. *J. Alloys Compd.* **2009**, *479*, 561–568. [[CrossRef](#)]

6. Chen, T.; Li, X.; Wang, H.; Yan, X.; Wang, L.; Deng, B.; Qu, M. The Effect of Gradient Boracic Polyanion-Doping on Structure, Morphology, and Cycling Performance of Ni-rich $\text{LiNi}_{0.8}\text{Co}_{0.15}\text{Al}_{0.05}\text{O}_2$ Cathode Material. *J. Power Sources* **2018**, *374*, 1–11. [[CrossRef](#)]
7. Woo, S.U.; Park, B.C.; Yoon, C.S.; Myung, S.T.; Prakash, J.; Sun, Y.K. Improvement of Electrochemical Performances of $\text{LiNi}_{0.8}\text{Co}_{0.1}\text{Mn}_{0.1}\text{O}_2$ Cathode Materials by Fluorine Substitution. *J. Electrochem. Soc.* **2007**, *154*, A649–A655. [[CrossRef](#)]
8. Becker, D.; Borner, M.; Nolle, R.; Diehl, M.; Klein, S.; Rodehorst, U.C.; Placke, T. Surface Modification of Ni-rich $\text{LiNi}_{0.8}\text{Co}_{0.1}\text{Mn}_{0.1}\text{O}_2$ Cathode Material by Tungsten Oxide Coating for Improved Electrochemical Performance in Lithium Ion Batteries. *ACS Appl. Mater. Interfaces* **2019**, *11*, 18404–18414. [[CrossRef](#)]
9. Konishi, H.; Yoshikawa, M.; Hirano, T. The Effect of Thermal Stability for High Ni-Content Layer-Structured Cathode Materials, $\text{LiNi}_{0.8}\text{Mn}_{0.1-x}\text{Co}_{0.1}\text{Mo}_x\text{O}_2$ ($x = 0, 0.02, 0.04$). *J. Power Sources* **2013**, *244*, 23–28. [[CrossRef](#)]
10. Chen, M.; Zhao, E.; Chen, D.; Wu, M.; Han, S.; Huang, Q.; Yang, L.; Xiao, X.; Hu, Z. Decreasing Li/Ni Disorder and Improving the Electrochemical Performances of Ni-rich $\text{LiNi}_{0.8}\text{Co}_{0.1}\text{Mn}_{0.1}\text{O}_2$ by Ca Doping. *Inorg. Chem.* **2017**, *56*, 8355–8362. [[CrossRef](#)]
11. Song, B.; Li, W.; Oh, S.M.; Manthiram, A. Long-Life Nickel-Rich Layered Oxide Cathodes with a Uniform Li_2ZrO_3 Surface Coating for Lithium-Ion Batteries. *ACS Appl. Mater. Interfaces* **2017**, *9*, 9718–9725. [[CrossRef](#)]
12. Schipper, F.; Bouzaglo, H.; Dixit, M.; Erickson, E.M.; Weigel, T.; Talianker, M.; Grinblat, J.; Erk, C. From Surface ZrO_2 Coating to Bulk Zr Doping by High Temperature Annealing of Nickel-Rich Lithiated Oxides and Their Enhanced Electrochemical Performance in Lithium Ion Batteries. *Adv. Energy Mater.* **2018**, *8*, 1701682. [[CrossRef](#)]
13. Min, K.; Park, K.; Park, S.Y.; Seo, S.W.; Choi, B.; Cho, E. Improved Electrochemical Properties of $\text{LiNi}_{0.91}\text{Co}_{0.06}\text{Mn}_{0.03}\text{O}_2$ Cathode Material via Li-Reactive Coating with Metal Phosphates. *Sci. Rep.* **2017**, *7*, 7151. [[CrossRef](#)] [[PubMed](#)]
14. Kim, U.; Myung, S.T.; Yoon, C.S.; Sun, Y.K. Extending the Battery Life Using an Al-Doped $\text{Li}[\text{Ni}_{0.76}\text{Co}_{0.09}\text{Mn}_{0.15}]\text{O}_2$ Cathode with Concentration Gradients for Lithium Ion Batteries. *ACS Energy Lett.* **2017**, *2*, 1848–1854. [[CrossRef](#)]
15. Ryu, H.H.; Park, K.J.; Yoon, C.S.; Sun, Y.K. Capacity Fading of Ni-Rich $\text{Li}[\text{Ni}_x\text{Co}_y\text{Mn}_{1-x-y}]\text{O}_2$ ($0.6 \leq x \leq 0.95$) Cathodes for High-Energy-Density Lithium-Ion Batteries: Bulk or Surface Degradation. *Chem. Mater.* **2018**, *30*, 1155–1163. [[CrossRef](#)]
16. Lim, J.M.; Hwang, T.; Kim, D.; Park, M.S.; Cho, K.; Cho, M. Intrinsic Origins of Crack Generation in Ni-Rich $\text{LiNi}_{0.8}\text{Co}_{0.1}\text{Mn}_{0.1}\text{O}_2$ Layered Oxide Cathode Material. *Sci. Rep.* **2017**, *7*, 39669. [[CrossRef](#)]
17. Kim, J.H.; Kim, Y.N.; Cho, S.M.; Wang, H.; Manthiram, A. Electrochemical Characterization of $\text{YBaCo}_3\text{ZnO}_7 + \text{Gd}_{0.2}\text{Ce}_{0.8}\text{O}_{1.9}$ Composite Cathodes for Intermediate Temperature Solid Oxide Fuel Cells. *Electrochim. Acta* **2010**, *55*, 5312–5317. [[CrossRef](#)]
18. Medvedev, D.; Lyagaeva, J.; Vdovin, G.; Beresnev, S.; Demin, A.; Tsiakaras, P. A Tape Calendering Method as an Effective Way for the Preparation of Proton Ceramic Fuel Cells with Enhanced Performance. *Electrochim. Acta* **2016**, *210*, 681–688. [[CrossRef](#)]
19. Bhat, M.A.; Zargar, R.A.; Modi, A.; Arora, M.; Gaur, N.K. Structural, Electrical and Magnetic Features of Kagomé YBaCo_4O_7 System. *Mater. Sci. Pol.* **2016**, *34*, 786–793. [[CrossRef](#)]
20. Tsvetkov, D.S.; Pralong, V.; Tsvetkova, N.S.; Zuev, A.Y. Oxygen Content and Thermodynamic Stability of $\text{YBaCo}_4\text{O}_{7\pm\delta}$. *Solid State Ion.* **2015**, *278*, 1–4. [[CrossRef](#)]
21. Lai, K.Y.; Manthiram, A. Phase Stability, Oxygen-Storage Capability, and Electrocatalytic Activity in Solid Oxide Fuel Cells of $(\text{Y}, \text{In}, \text{Ca})\text{BaCo}_{4-y}\text{Ga}_y\text{O}_{7+\delta}$. *Chem. Mater.* **2016**, *28*, 9077–9087. [[CrossRef](#)]
22. Shin, J.-S.; Park, H.; Park, K.; Saqib, M.; Jo, M.; Kim, J.H.; Lim, H.-T.; Kim, M.; Kim, J.; Park, J.-Y. Activity of Layered Swedenborgite Structured $\text{Y}_{0.8}\text{Er}_{0.2}\text{BaCo}_{3.2}\text{Ga}_{0.8}\text{O}_{7+\delta}$ For Oxygen Electrode Reactions in at Intermediate Temperature Reversible Ceramic Cells. *J. Mater. Chem. A* **2021**, *9*, 607–621. [[CrossRef](#)]
23. Goktepe, H.; Sahan, H.; Ulgen, A.; Patat, S. Synthesis and Electrochemical Properties of Carbon-Mixed $\text{LiEr}_{0.02}\text{Fe}_{0.98}\text{PO}_4$ Cathode Material for Lithium-Ion Batteries. *J. Mater. Sci. Technol.* **2011**, *27*, 861–864. [[CrossRef](#)]
24. Liu, S.; Zhao, H.; Tan, M.; Hu, Y.; Shu, X.; Zhang, M.; Chen, B.; Liu, X. Er-Doped $\text{LiNi}_{0.5}\text{Mn}_{1.5}\text{O}_4$ Cathode Material with Enhanced Cycling Stability for Lithium-Ion Batteries. *Materials* **2017**, *10*, 859. [[CrossRef](#)]
25. Liu, Z.; Li, J.; Zhu, M.; Wang, L.; Kang, Y.; Dang, Z.; Yan, J. Enhanced Structural Stability and Electrochemical Performance of $\text{LiNi}_{0.6}\text{Co}_{0.2}\text{Mn}_{0.2}\text{O}_2$ Cathode Materials by Ga Doping. *Materials* **2021**, *14*, 1816. [[CrossRef](#)]
26. Parkkima, O.; Karppinen, M. The $\text{YBaCo}_4\text{O}_{7+\delta}$ -Based Functional Oxide Material Family: A Review. *Eur. J. Inorg. Chem.* **2014**, 4056–4067. [[CrossRef](#)]
27. Kim, J.-H.; Manthiram, A. Low Thermal Expansion $\text{RBa}(\text{Co},\text{M})_4\text{O}_7$ Cathode Materials Based on Tetrahedral-Site Cobalt Ions for Solid Oxide Fuel Cells. *Chem. Mater.* **2010**, *22*, 822–831. [[CrossRef](#)]
28. Kim, J.H.; Park, K.J.; Kim, S.J.; Yoon, C.S.; Sun, Y.K. A Method of Increasing the Energy Density of Layered Ni-Rich $\text{Li}[\text{Ni}_{1-2x}\text{Co}_x\text{Mn}_x]\text{O}_2$ cathodes ($x = 0.05, 0.1, 0.2$). *J. Mater. Chem. A* **2019**, *7*, 2694–2701. [[CrossRef](#)]
29. Choi, W.; Shin, H.C.; Kim, J.M.; Choi, J.Y.; Yoon, W.S. Modeling and Applications of Electrochemical Impedance Spectroscopy (EIS) for Lithium-Ion Batteries. *J. Electrochem. Sci. Technol.* **2020**, *11*, 1–13. [[CrossRef](#)]
30. Beak, M.; Park, S.; Kim, S.; Park, J.; Jeong, S.; Thirumalraj, B.; Jeong, G.; Kim, T.; Kwon, K. Effect of Na from the Leachate of Spent Li-Ion Batteries on the Properties of Resynthesized Li-Ion Battery Cathodes. *J. Alloys Compd.* **2021**, *873*, 159808–159816. [[CrossRef](#)]
31. Jeong, S.; Park, S.; Beak, M.; Park, J.; Shon, J.-S.; Kwon, K. Effect of Residual Trace Amounts of Fe and Al in $\text{Li}[\text{Ni}_{1/3}\text{Mn}_{1/3}\text{Co}_{1/3}]\text{O}_2$ Cathode Active Material for the Sustainable Recycling of Lithium-Ion Batteries. *Materials* **2021**, *14*, 2464. [[CrossRef](#)] [[PubMed](#)]
32. Shaju, K.M.; Rao, G.V.S.; Chowdari, B.V.R. Electrochemical Kinetic Studies of Li-ion in O_2 -Structured $\text{Li}_{2/3}(\text{Ni}_{1/3}\text{Mn}_{2/3})\text{O}_2$ and $\text{Li}_{(2/3)+x}(\text{Ni}_{1/3}\text{Mn}_{2/3})\text{O}_2$ by EIS and GITT. *J. Electrochem. Soc.* **2003**, *150*, A1–A13. [[CrossRef](#)]

33. Zheng, J.M.; Shi, W.; Gu, M.; Xiao, J.; Zuo, P.J.; Wang, C.M.; Zhang, J.G. Electrochemical Kinetics and Performance of Layered Composite Cathode Material $\text{Li}[\text{Li}_{0.2}\text{Ni}_{0.2}\text{Mn}_{0.6}]\text{O}_2$. *J. Electrochem. Soc.* **2013**, *160*, A2212–A2219. [[CrossRef](#)]
34. Peng, F.W.; Mu, D.Y.; Li, R.H.; Liu, Y.L.; Ji, Y.P.; Dai, C.S.; Ding, F. Impurity Removal with Highly Selective and Efficient Methods and the Recycling of Transition Metals from Spent Lithium-Ion Batteries. *RSC Adv.* **2019**, *9*, 21922–21930. [[CrossRef](#)]
35. Shaju, K.M.; Rao, G.V.S.; Chowdari, B.V.R. EIS and GITT Studies on Oxide Cathodes, $\text{O}_2\text{-Li}_{(2/3)+x}(\text{Co}_{0.15}\text{Mn}_{0.85})\text{O}_2$ ($x = 0$ and $1/3$). *Electrochim. Acta* **2003**, *48*, 2691–2703. [[CrossRef](#)]